Marinetto, E., et al. (2017). Integration of free-hand 3D ultrasound and mobile C-arm cone-beam CT: Feasibility and characterization for real-time guidance of needle insertion, *Computerized Medical Imaging and Graphics*, v. 58, pp.: 13-22.

DOI: https://doi.org/10.1016/j.compmedimag.2017.03.003

Available online at www.sciencedirect.com

SciVerse ScienceDirect

Integration of Free-Hand 3D Ultrasound and Mobile C-Arm Cone-Beam CT: Feasibility and Characterization for Real-Time Guidance of Needle Insertion

E. Marinetto,[a,b] A. Uneri,[c] T. De Silva,[b] S. Reaungamornrat,[c] W. Zbijewski,[b] A. Sisniega,[b] S. Vogt,[d] G. Kleinszig,[d] J. Pascau,[a] J. H. Siewerdsen[b,c*]

a Dept. Bioingeniería e Ingeniería Aeroespacial. Universidad Carlos III de Madrid. Instituto de Investigación Sanitaria Gregorio Marañón, Madrid, Spain
b Department of Biomedical Engineering, Johns Hopkins University, Maryland, USA
c Department of Computer Science, Johns Hopkins University, Baltimore, USA
d Siemens Healthcare XP Division, Erlangen, Germany

Abstract

This work presents development of an integrated ultrasound (US) – cone-beam CT (CBCT) system for image-guided needle interventions, combining a low-cost ultrasound system (Interson VC 7.5 MHz, Pleasanton CA) with a mobile C-arm for fluoroscopy and CBCT via use of a surgical tracker. Imaging performance of the ultrasound system was characterized in terms of depth-dependent contrast-to-noise ratio (CNR) and spatial resolution. US-CBCT system was evaluated in phantom studies simulating three needle-based procedures: drug delivery, tumor ablation, and lumbar puncture. Low-cost ultrasound provided flexibility but exhibited modest CNR and spatial resolution that is likely limited to fairly superficial applications within a ~10 cm depth of view. Needle tip localization demonstrated target registration error 2.1–3.0 mm using fiducial-based registration.

Ultrasound; cone-beam CT; C-arm imaging; image-guided procedures; target registration error

* Corresponding author. Tel.: +1443-287-6269.
E-mail address: jeff.siewerdsen@jhu.edu.

1. Introduction

Accurate placement of a needle or probe is a common requirement in minimally invasive interventions, pain management, and drug delivery. In brachytherapy for example, radioactive seeds need to be precisely placed within the patient to ensure correct delivery of the planned dose distribution to the tumor volume (Koukourakis et al., 2009). Various ablation techniques rely on similar accurate placement of therapeutic probes within the target – e.g., radiofrequency ablation (RFA) and cryotherapy (Tiong and Maddern, 2011). Accurate placement of the needle / probe is therefore important to achieving the clinical objective and avoiding complications such as infection (Rudzinski and Kawakami, 2014), hemorrhage, pain, or pneumothorax (Boskovic et al., 2014).

Interventional imaging systems are widely used to assist clinicians during needle insertion and improve safety and accuracy of the procedure (CHIN et al., 2008; Cleary and Peters, 2010; Koukourakis et al., 2009). Two-dimensional ultrasound is commonly used to provide real-time imaging at a relatively low cost (Fingerman et al., 2009; Lamperti et al., 2012; MD et al., 2014). Example low-cost ultrasound systems include those produced by Interson (Pleasanton USA), Wallach Surgical Devices (Trumbull CT USA), and American 3B Scientific (Tucker Georgia USA), offering a diversity of designs adapted to specific applications, such as vascular drug delivery or percutaneous biopsy. However, manufacturers usually offer fairly limited information regarding imaging performance characteristics, and rigorous technical assessment is valuable to both researchers and clinicians in knowledgably selecting a low-cost system suitable to a particular task. In particular, real-time ultrasound visualization of the needle position and orientation relative to surrounding anatomy can be helpful in facilitating needle guidance (Nolsøe et al., 1990) (Zhu et al., 2007); however, safe and accurate needle placement requires sufficient spatial for accurate targeting, contrast resolution for visualization of the target of interest (e.g., cyst or vessel), and depth of field for the anatomical site of interest.

Registering anatomical information from high-resolution 3D preoperative imaging such as computed tomography (CT) or magnetic resonance imaging (MRI) to the intraoperative scene could improve localization accuracy in such interventions. These imaging techniques provide soft-tissue contrast and high spatial resolution with a large 3D field of view, for example, CT guidance of RFA was shown to achieve probe localization error <3 mm (Maier-Hein et al., 2008). However, these modalities carry strong requirements / limitations in cost, room site considerations, radiation dose, real-time imaging capability, and ease of use. On the other hand, in (Yaniv et al., 2010), the authors present a cone-beam CT (CBCT) and fluoroscopy system capable of guiding needle-based interventions including vertebroplasty, RFA of large lung tumors, and lung biopsies. Such work demonstrates the benefits of intraoperative CBCT with respect to radiation dose reduction, as it required only a single CBCT at the beginning of the procedure showing a mean overall targeting error of 3.7 ± 2.3 mm (Yaniv et al., 2010). Many image guidance applications require up-to-date imaging of the patient during the procedure, and the combination of US and CBCT could present a useful approach – the former offering real-time slice and volume updates without radiation, and the latter providing fluoroscopy volumetric imaging on demand. Some needle-based applications, such as low-dose rate (LDR) or high-dose-rate (HDR) brachytherapy where needles are introduced into the patient anatomy to deliver radiation interstitially, would benefit from an anatomically updated CBCT image – both for guidance of needle / seed placement and for calculation of the dose distribution (Showalter et al., 2016). Similarly, in (Roeder et al., 2010), authors evaluated the feasibility of using a C-arm to acquire images during IOERT in order to calculate a 3D dose distribution based on individual patient anatomy, which is not possible on US images. Although intraoperative 3D imaging provided rich anatomical context, as the authors discuss, the lack of real-time imaging during needle placement carries the potential for inaccurate target localization due to respiratory motion and anatomical deformation (Bachar et al., 2007; Barker et al., 2009; Chan et al., 2008; Khoury et al., 2007; Lee et al., 2012).

Recent improvements in the cost, image quality, and flexibility in use of low-cost ultrasound imaging systems along with the increasing availability of mobile C-arm CBCT motivates a multi-modality 2D and 3D imaging. The combination of ultrasound and mobile C-arm CBCT could provide up-to-date anatomical visualization and allow precise localization of interventional tools registered through surgical tracking systems and/or image registration (Uneri et al., 2012). The objective of this work is to present initial development of an integrated ultrasound-CBCT system for image-guided needle interventions, combining a surgical navigation system with a low-cost transducer for real-time free-hand ultrasound and a mobile C-arm for fluoroscopy and CBCT. The ultrasound probe used in these studies was the Interson Vascular Access Probe VC 7.5 MHz (Interson, Pleasanton CA), and the work includes assessment of ultrasound imaging performance characteristics – to our knowledge, the first reported assessment for this device. We also integrated the probe with the TREK navigation platform (Uneri et al., 2012) via the manufacturer's software development kit (SDK) and the PLUS library (Lasso et al., 2014). The mobile C-arm was a previously reported (Daly et al., 2008; Schafer et al., 2012, 2011; Wermker et al., 2014) prototype capable of fluoroscopy and CBCT. The performance of ultrasound-CBCT registration was investigated in three simulated needle guidance scenarios in phantoms emulating vascular access, abdominal tumor ablation, and lumbar puncture procedures.

2. Material and Methods

2.1. Ultrasound Imaging Performance

An Interson Vascular Access Probe VC 7.5 MHz (Interson, Pleasanton CA) (Fig. 1a) was used as the basis for ultrasound-CBCT integration for image-guided needle insertion. This low-cost probe allows imaging at three frequencies (5, 7.5 and 12 MHz) with a manufacturer-specified depth range from 5 to 100 mm. The focal point is specified to be 20 mm from the transducer, and the scan sector has a 60° aperture. The probe can be operated simply via a single USB connection to a tablet, laptop, or workstation without an extra power supply. As detailed below, the ultrasound probe was assessed in terms of its imaging performance characteristics, geometric accuracy of surgical tracking and image registration with CBCT.

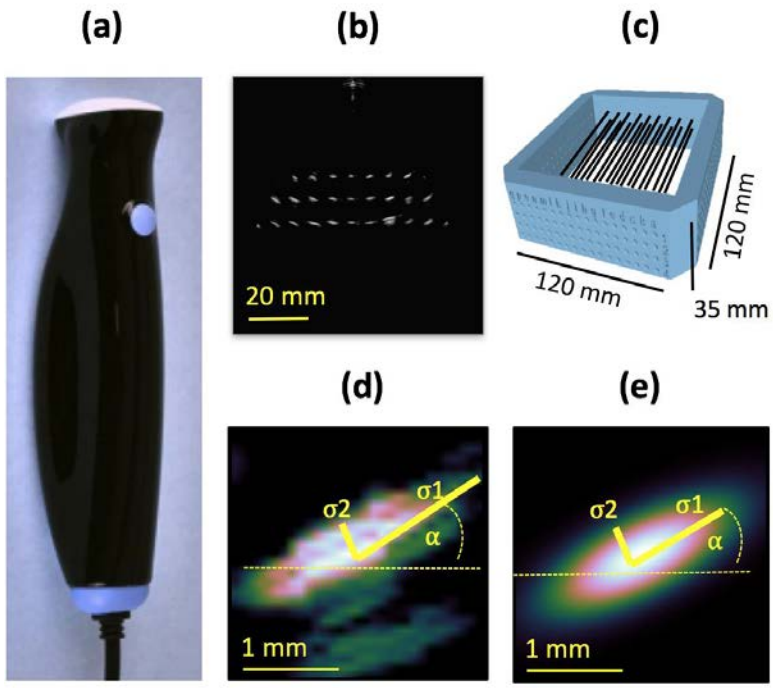

Fig 1. Ultrasound probe and PSF assessment. (a) Interson 7.5 MHz ultrasound probe (Interson, Pleasanton USA). (b) Example ultrasound image of the wire phantom. (c) 3D model of the wire phantom used for PSF assessment. (d) Example image showing the intersection of a wire with the ultrasound image plane. (e) Gaussian fit and parameters for the image shown in (d).

2.1.1. Ultrasound Image Quality

Image quality of the ultrasound system was assessed in terms of spatial resolution and contrast-to-noise ratio (CNR) measured at different probe frequency settings and as a function of depth in the field of view (FOV). To evaluate spatial resolution, we used the phantom shown in Fig. 1c, constructed using a 3D printer (and polylactic acid material) and consisting of four walls with holes placed at different heights similar to the calibration phantom described in (Neshat et al., 2013). Nylon wires of 0.5 mm diameter were spatially separated by 5 mm (Fig. 1b). An example ultrasound image is shown in Fig. 1b, where the intersections of the wires and the ultrasound image plane are detected. These intersections were localized and fit to a bivariate Gaussian (Eq. 1) as follows:

$$\mathrm{G}(x,y) = \frac{1}{2\pi\sigma_1\sigma_2}\exp(-[a(x-\mu_1)^2 - 2b(x-\mu_1)(y-\mu_2) + c(y-\mu_2)^2])$$
$$a = \frac{cos^2\alpha}{2\sigma_1^2} + \frac{sin^2\alpha}{2\sigma_2^2}$$
$$b = -\frac{\sin 2\alpha}{4\sigma_1^2} + \frac{\sin 2\alpha}{4\sigma_2^2} \quad (1)$$
$$c = \frac{sin^2\alpha}{2\sigma_1^2} + \frac{cos^2\alpha}{2\sigma_2^2}$$

where μ_1, μ_2 localizes the centroid (corresponding to the voxel with maximum image intensity μ_X, μ_Y), σ_1 and σ_2 are the standard deviation of the Gaussian, and ($|\alpha| < \frac{\pi}{3}$ is the angle between the centre line of the ultrasound

image plane and the line that pass through the point at which the point spread function (PSF) is measured and the probe sensor. The two-dimensional PSF was estimated in both directions (σ_1 and σ_2) as the full-width at half-maximum FWHM $= 2\sqrt{2\ln 2}\,(\sigma_1, \sigma_2)$ .For each intersection we estimated σ_1, σ_2, and α as shown in Fig. 1d,e.

We acquired 200 image planes with the ultrasound probe held in a static passive arm for each combination of the operating frequencies (5, 7.5, and 12 MHz) and depths (50, 60, 80, 100 and 120 mm) at a constant frame rate of 5 fps. The σ_1, σ_2, and α parameters were evaluated for each case as a function of position in the FOV.

To measure the CNR we constructed a phantom that emulated a soft tissue background with blood vessels as shown in Fig 3a. Gelatin and cylindrical pasta were used to mimic the properties of soft-tissue and blood vessels, respectively. Simulated vessels were placed at varying depth within an otherwise uniform simulated soft-tissue background. The CNR in ultrasound images was measured in terms of the contrast between the simulated vessels and the background as a function of depth using regions of interest (ROI) containing the simulated vessel and background with a 5×5 pixel size. CNR was computed from each ROI as:

$$\mathrm{CNR} = 2\frac{\mu_v - \mu_{bg}}{\sigma_v + \sigma_{bg}} \tag{2}$$

where μ_v is the mean intensity value of the simulated vessel wall, μ_{bg} is the mean intensity value of the background, σ_v is the standard deviation of voxel values in the vessel wall, and σ_{bg} is the standard deviation of voxels in the background. For each measurement, we acquired 500 ultrasound images at 5 fps at operating frequencies of 5, 7.5 and 12 MHz.

2.1.2. Ultrasound Calibration

The ultrasound probe was calibrated in terms of spatial location and timing of the acquisition. Temporal and spatial calibration of the tracked ultrasound probe is necessary for free-hand 3D ultrasound imaging (via image mosaic) and surgical navigation (Lasso et al., 2014). Temporal calibration estimates the time lag between acquisition of the ultrasound images and the pose information read from a surgical tracking system, thereby allowing synchronization of the ultrasound and tracking systems. Spatial calibration is then used to estimate the transformation (${}^{P}T_{U}$) from the ultrasound image plane (labelled U in Fig. 2c) to the tracked rigid body used to localize the probe (labelled P in Fig. 2c). In Fig. 2c all related transformations are depicted, where each transformation, ${}^{B}T_{A}$, is a transformation from 'A' to 'B' frames. Using ${}^{P}T_{U}$, the ultrasound image plane localized in the tracker coordinate system can be calculated as

$$\langle {}^{T}T_{U} \rangle = {}^{T}T_{P}\,{}^{P}T_{U} \tag{3}$$

where ${}^{T}T_{P}$ is the pose of the rigid-body probe (P) in the tracker frame (T), and $\langle {}^{T}T_{U} \rangle$ is the estimated transformation from the ultrasound image to the tracker geometric frame.

The PLUS open-source software toolkit (Lasso et al., 2014) – originally developed for ultrasound-guided interventions – was used to integrate the Interson software development kit (SDK) with the TREK surgical tracking and navigation platform (Uneri et al., 2012), using essential functions for tracked ultrasound, such as spatial calibration, ultrasound image acquisition, free-hand 3D ultrasound volume imaging via mosaic (referred to as "mosaicking").

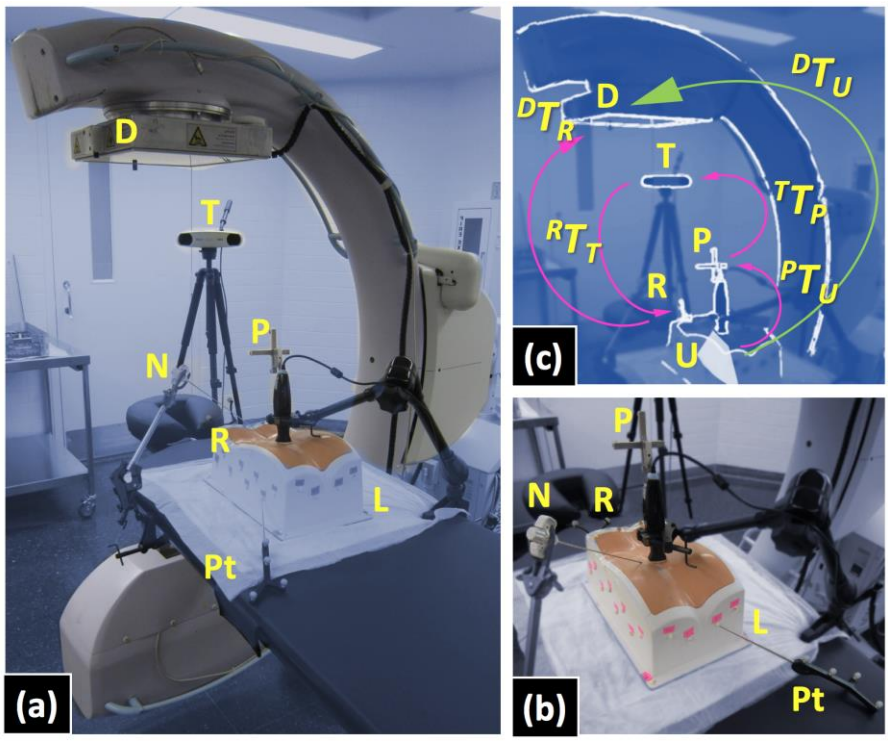

Fig. 2. Experimental setup for free-hand 3D ultrasound imaging with C-Arm CBCT and surgical tracking for guidance of needle placement in a lumbar phantom (panels a and b). Panel (c) shows pertinent coordinate transformations for needle guidance. System components include: C-Arm flat-panel detector (D), Polaris Vicra tracker (T), ultrasound probe with attached rigid body for tracking (P), lumbar phantom (L), phantom tracking reference marker (R), Polaris pointer used for divot localization (Pt), surgical needle (N) and ultrasound image plane (U).

The calibration transformation (${}^{P}T_{U}$) was obtained from imaging a calibration phantom via a tracked ultrasound. In this work, we employed the calibration 'fCal 2.0 Phantom' proposed by PLUS authors (Lasso et al., 2014) for 100–120 mm depth ultrasound image settings. The calibration phantom was formed using nine lengths of nylon line whose relative spatial positions are known. A description of the phantom and a printable 3D model can be obtained from the public web documentation for the PLUS library (Lasso et al., 2014). The calibration transformation (${}^{P}T_{U}$) is estimated by the algorithm presented in (Carbajal et al., 2013) that extracts the pose of the wire intersection within image planes and minimizes the in-plane error (IPE), computed as the least-square difference of the detected and expected intersections of the wires and the ultrasound image plane.

$$\text{IPE} = \sum_{i=1}^{N_i} \sum_{j=1}^{N_w} \left\| u_{x_{ij}} - u_{w_{ij}} \right\|^2 \tag{4}$$

where $u_{x_{ij}}$ is the detected intersection between the j[th] wire and the i[th] ultrasound image, and $u_{w_{ij}}$ is the expected intersection position of the j[th] wire with the computed image plane.

The aim of the calibration assessment presented below was to determine the minimum number of image planes (N_i) required for an accurate spatial calibration of the ultrasound probe. We performed 10 repeated spatial

calibrations using different number of ultrasound plane images (100, 150, 200, 250, 500 and 750). For evaluation, we acquired an extra set of images (20% of the number of calibration images) and measured the average IPE on this extra set.

2.2. Ultrasound and C-Arm Cone-Beam CT Integration

The integration of ultrasound image acquisition and C-arm CBCT was implemented using the TREK imaging and surgical navigation platform (Uneri et al., 2012). TREK is based primarily on two software packages: cisst (Johns Hopkins University, Baltimore MD) (Deguet et al., 2008) and 3D Slicer (Brigham and Women's Hospital, Boston MA) (Pieper et al., 2004) allowing intraoperative CBCT and image guidance (Uneri et al., 2012). In this work, we contributed two main software developments: (1) TREK functionality was expanded to perform ultrasound imaging by means of the PLUS toolkit, and (2) a dedicated module was created for ultrasound imaging that permits control of the acquisition parameters (i.e., operating probe depth and frequency), loading of tracker calibration files (calibration transformation), and custom ultrasound scanner functionalities (i.e., last-image-hold, changing modes, and FOV settings). The PLUS toolkit interfaces to the probe using the manufacturer's SDK and a software wrapper that permits the PLUS library to call SDK functions. However, this wrapper does not allow real-time ultrasound image acquisition nor changing ultrasound acquisition parameters. This work contributed such functionality to the PLUS toolkit and can be found in the most recent version of the code contribution to the wrapper in (Kitware Inc., n.d.).

The C-arm imaging platform was the prototype mobile isocentric C-arm for intraoperative CBCT shown in Fig. 2 (D, a modified PowerMobil, Siemens, Erlangen, Germany, as described in (Dang et al., 2012; Hamming et al., 2009; Siewerdsen et al., 2005; Wang et al., 2014)) equipped with a flat-panel detector (PaxScan 3030 +, 1536×1536 pixels at 194 μm pitch), Varian Imaging Products, Palo Alto, CA. The C-arm is able to rotate about the operating room (OR) table covering a total angular range of ~178° and operates in pulsed-fluoroscopic mode allowing 3D CBCT volume reconstruction with a ~20×20×20 cm^3 FOV. The ultrasound-CBCT system can be used with other probes that are supported by PLUS and may be tailored to other specific clinical applications.

An experimental setup was devised to evaluate the feasibility and integration of the system (Fig. 2). We placed the mobile C-arm (Fig. 2, D) tableside in a laboratory OR. We placed an optical tracker (Polaris Vicra, Mississauga Canada) (Fig. 2, T) ~1.5 m from the operating table, allowing C-arm rotation and line-of-sight to the tracked elements (i.e., ultrasound probe, assessment phantoms and a pointer). The ultrasound probe was temporally and spatially calibrated (using 500 calibration frames) before experimental assessment with a mean IPE of ~1.2 mm.

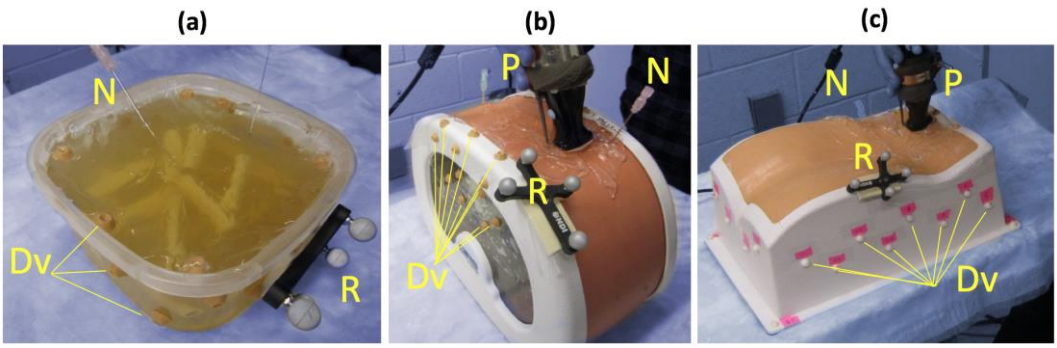

Fig. 3. Validation phantoms: vessel phantom (a), abdominal soft-tissue phantom (b) and lumbar phantom (c). Attached optical tracked reference frame (R), inserted surgical needles (N), registration 3D printed divots (Dv) and ultrasound probe during acquisition (P).

Experiments employed three phantoms: a custom soft-tissue (gelatin) simulated vessel phantom (described before, Fig. 3a), an abdominal phantom (Image-guided Abdominal Biopsy Phantom, Model 071A, CIRS, Norfolk, Virginia, USA) with simulated spherical tumors of varying density (Fig. 3b), and a lumbar spine phantom (Lumbar Training Phantom, Model 034, CIRS, Norfolk, Virginia, USA) containing simulated bone, cerebrospinal fluid, and soft tissues (Fig. 3c). Fiducial divots (Fig. 3, Dv) were placed on the surface of each phantom to register the free-hand ultrasound and CBCT images via point-based registration. Two rigid needles of 22-gauge (Fig. 2 and 3, N) were inserted at different locations within the CBCT FOV, targeting an interior vessel (~0.5 cm diameter), simulated tumor (~1 cm diameter), and facet joint (~0.5 cm width) in the three phantoms, respectively, in order to simulate three needle-based procedures (drug delivery, tumor ablation, and lumbar puncture).

The experimental workflow consisted of the following steps: (1) the 3D fiducial locations were measured using a tracked pointer (Fig. 2, Pt) in the tracker geometric space, which coincides with the US free-hand space after calibration (Sec. 2.1.2); (2) three free-hand 3D ultrasound images were acquired following initial CBCT; (3) US- and CBCT- guided procedure simulation (needle insertion); and (4) acquisition of CBCT and three free-hand 3D ultrasound images (for each phantom study) at the end of the procedure with needles at target locations inside a given phantom.

Fiducial divots were segmented in the first CBCT image as reference and localized in the tracker coordinate frame using a tracked pointer tool (Fig. 2, Pt). Localization in both frames were registered using point-based registration to obtain the registration matrix ${}^{D}T_{R}$ (Fig. 2c) that relates CBCT and tracker frames. Using ${}^{D}T_{R}$ and ${}^{P}T_{U}$ we estimated the transformation between CBCT and free-hand 3D ultrasound as:

$$\langle {}^{D}T_{U} \rangle = {}^{D}T_{R}\, {}^{R}T_{T}\, {}^{T}T_{P}\, {}^{P}T_{U} \tag{5}$$

The geometric point-based registration accuracy was evaluated in terms of fiducial registration error (FRE) and target registration error (TRE). FRE was measured for each registration as:

$$\langle \mathrm{FRE} \rangle = \sqrt{\sum_{i=1}^{N_{\mathrm{divots}}} \left\| x_{\mathrm{Tracker}(i)} - x_{\mathrm{CBCT}(i)} \right\|^{2}} \tag{6}$$

where $x_{\mathrm{Tracker}(i)}$ and $x_{\mathrm{CBCT}(i)}$ are the pose of the i$^{\mathrm{th}}$ divot in the tracker (free-hand 3D ultrasound image) and in the CBCT image frames, respectively. N_{divots} is the number of divots used for each study (20, 13, and 23 in the vessel, abdomen, and lumbar, respectively). Estimation of TRE was performed by localizing the inserted needle tip in free-hand 3D ultrasound and CBCT images manually by three users that were familiar with CT and US manual segmentation. For each registration the TRE was estimated as:

$$\langle \mathrm{TRE} \rangle = \sum_{i=1}^{3} \sum_{j=1}^{2} \left\| y_{\mathrm{3DUS}(i,j)} - y_{\mathrm{CBCT}(i,j)} \right\| \tag{7}$$

where $y_{3\mathrm{DUS}(i,j)}$ and $y_{\mathrm{CBCT}(i,j)}$ are the pose of the localized j[th] needle tip in the acquired i[th] 3D ultrasound and CBCT image respectively.

2.3. Image-based registration assessment

Image-based registration could further improve registration accuracy, and enable compensation for misalignment caused by patient motion during the procedure. However, it requires a robust image similarity metric suitable for ultrasound-CBCT image registration. Challenges associated with such images and similarity metrics include: the need for a fast performance; untracked (void) regions within 3D ultrasound volume acquired via mosaicking of tracked 2D ultrasound; and limitations of ultrasound imaging in the context of gas-filled regions and/or bony structures. Registration of C-arm CBCT with other 3D imaging modalities has been previously reported and is the subject of ongoing work (Nithiananthan et al., 2012; Reaungamornrat et al., 2013; Uneri et al., 2013). Ultrasound-CT registration has also been investigated in, for example, (Brendel et al., 2002) and (Muratore et al., 2002), where authors addressed the limitation of ultrasound in scanning bony structures by surface-based registration techniques. The authors simulated ultrasound images from the CT scans to perform the registration in liver and kidney applications in (Wein et al., 2008). An example of image-based registration is described in (Yan et al., 2012) in which 2D ultrasound image planes were registered to CT volumes employing the cross correlation as similarity metric.

To investigate the feasibility of ultrasound-CBCT image registration in application to needle interventions, we implemented and assessed three classes of image similarity metric that could support such integration, including Normalized Mutual Information (NMI)

$$\mathrm{NMI} = \frac{H(F) + H(u(M,p))}{H(F, u(M,p))} \tag{8}$$

where $H(F)$ is the entropy of fixed image, $H(u(M,p))$ is the entropy of the moving image under a deformation u with transformation parameters p, and $H(F,u(M,p))$ is the joint entropy of images F and M. We also investigated performance using Normalized Cross Correlation (NCC)

$$\mathrm{NCC} = \frac{\sum_x F(x) * M(x + u(x,p))}{\sqrt{\sum_x F(x)^2 * M(x + u(x,p))^2}} \tag{9}$$

where x is a voxel in the fixed image F, M is the moving image, and $u\ (x,p)$ is the deformation of x depending on the transform parameters p. Finally, we measured the similarity of F and M using a Huber distance (Huber, 1964) between their modality-independent neighborhood descriptors (MIND) (Heinrich et al., 2013). An element of a MIND descriptor $S(I,x,y)$ is given by

$$S(I,x,y) = \exp\left(-\frac{SSD(x,y)}{\sigma^2}\right) \qquad x,y \in N \tag{10}$$

where I is the image, σ^2 is an estimate of the local variance at x, SSD is the sum of square differences, and N is the neighborhood over which the descriptor is calculated for a patch centered at x.

We defined a ROI of ~40×30×30 mm^3 inside the vessel phantom containing two whole vessels in order to evaluate the image-based metrics on a volume scanned by the free-hand 3D ultrasound imaging method described above. We randomly perturbed the ultrasound ROI volume from the tracker-based registration solution by a rigid transformation (translation and rotation) according to a Gaussian distribution:

$$\mathrm{G}(x) = \frac{1}{\sigma\sqrt{2\pi}} e^{\frac{-(x-\mu)^2}{2\sigma^2}} \tag{11}$$

where μ is the mean value (or perturbation factor) and $\sigma = 0.1$ is the standard deviation. We varied the perturbation factor over the μ range [-3,3] (mm and degrees for translation and rotation, respectively) in steps of 0.1. For each perturbation, we performed 100 trials with 6 random parameters corresponding to the 6 degrees of freedom of a rigid transformation.

Image-based registration performance was assessed in terms of TRE as well as the objective function (NCC, NMI, and MIND Huber distance) directly as a function of perturbation factor. The registration result was visualized by overlaying the gradient of the CBCT volume (moving target image) with the free-hand 3D ultrasound (fixed source image).

3. Results

3.1. Ultrasound Imaging Performance

The PSF for different frequency and depth is showed in Fig. 4a. An example of the PSF parameters [standard deviation in both directions (σ_1 ,σ_2) and angle (α)] for the case of 7.5 MHz frequency and 80 mm depth is depicted in Fig. 4b–d. The PSF was reduced (sharper) in the lateral direction for higher frequencies and almost constant in the ultrasound pulse propagation direction, consistent with the dependence of depth resolution on duration of the ultrasound pulse (independent of depth and frequency). Also notice in Fig. 4b (σ_1 map) that the minimum measured σ_1 is found at ~2 cm depth, which corresponds to the probe focal point according to manufacturer's specifications. The computed α map was consistent with the direction of the ultrasound pulse through the image plane. Overall, we see FWHM that is fairly constant (FWHM_2 ~0.3 mm) in the lateral direction and steeply degrading with depth (FWHM_1 ~1.0–4.5 mm) in the depth direction over the depth ranges 20–100 mm.

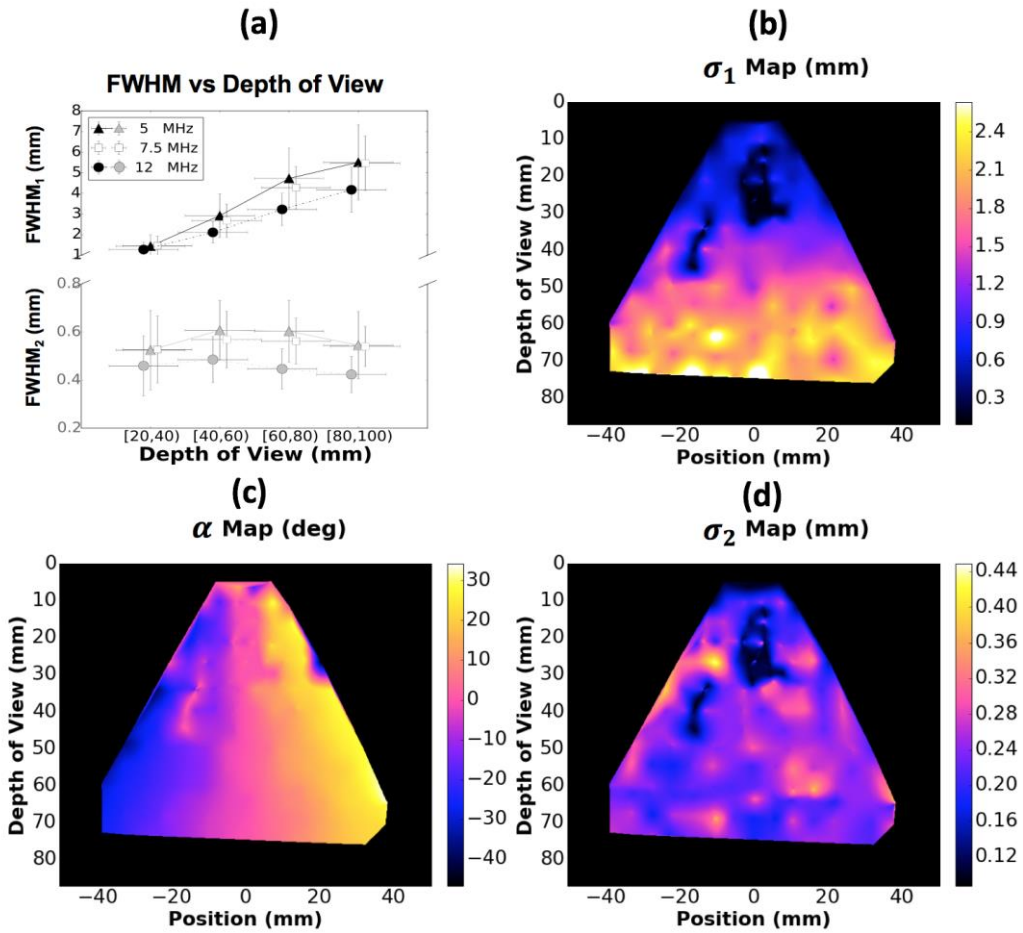

Fig. 4. Ultrasound image spatial resolution. (a) FWHM of the Point Spread Function (PSF) for different frequencies as a function of depth of view. (b) Measured PSF width at 7.5 MHz and maximum depth of 80 mm in the direction perpendicular to sound wave propagation. (c) Angle between the two-dimensional fitting Gaussian model with respect to horizontal. (d) Measured PSF width in the direction parallel to sound wave propagation direction.

The CNR measured at different frequencies as a function of depth is shown in Fig. 5. The CNR decreases by more than a factor of 2 over the depth of field and is highest at the lowest frequency settings (Fig. 5a). This degradation is also shown in the example ultrasound image of the vessel phantom (Fig. 5b) where CNR decreases along the length of the vessel wall as the ultrasound wave is attenuated at increased depth in tissue. Broadening of the lateral component of the PSF width at increased depth is also evident.

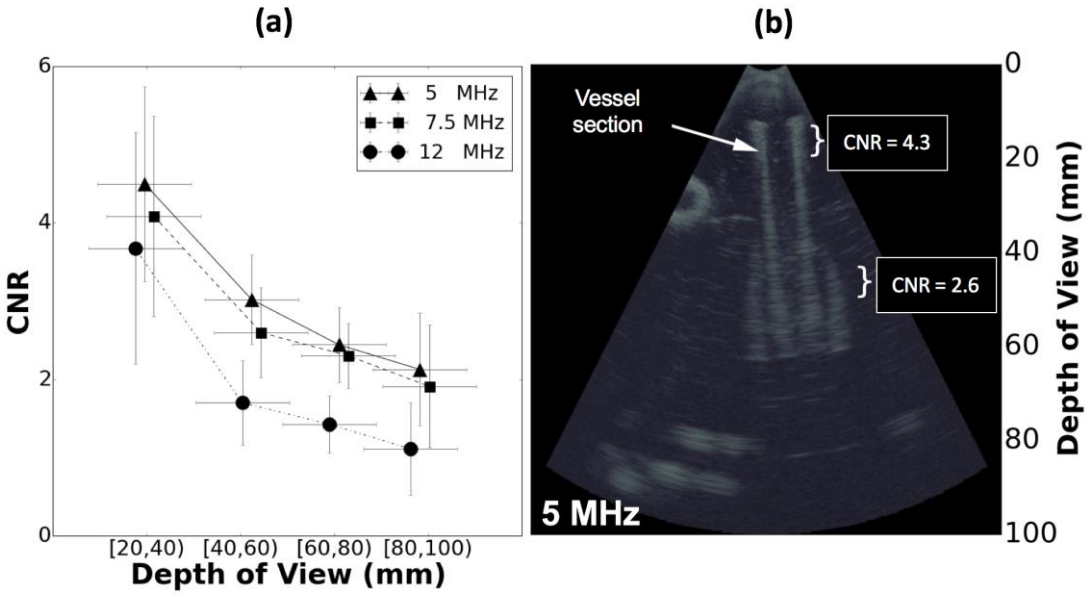

Fig. 5. Contrast resolution measurements for the ultrasound imaging system. (a) Mean and standard deviation in CNR for different frequencies as a function of depth. (b) Example ultrasound image of the vessel phantom acquired at 5 MHz and maximum depth of 100 mm.

Results for the ultrasound calibration assessment are presented in Fig 6. The IPE distribution is presented as a function of the number of frames used in the calibration, showing the degradation in IPE when the number of calibration images is small (<150). Using more than 500 frames for calibration does not seem to lead to lower IPE, and the minimum IPE is limited by the image resolution for greater than ~300 frames. In Fig. 6b a volumetric rendering of the vessel phantom is shown to illustrate the capability of the system to produce free-hand 3D ultrasound volumes when a correct calibration is achieved.

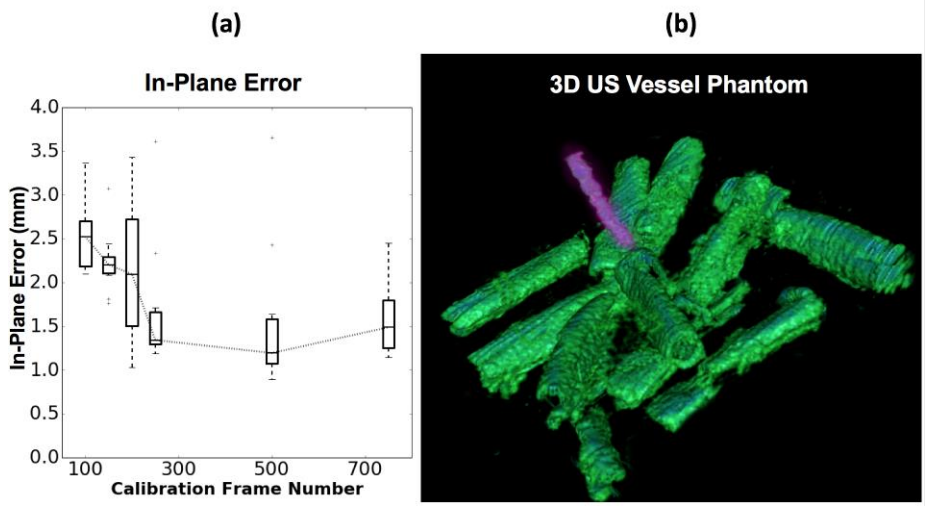

Fig. 6. Registration accuracy. (a) In-plane error during probe-to-tracker calibration as a function of the number of collected calibration frames. (b) Volumetric rendering of the vessel phantom 3D ultrasound image showing the simulated vessels (green) and the inserted surgical

needle (purple).

3.2. Ultrasound and C-Arm Cone-Beam CT Integration

The TREK navigation system updated via the PLUS software library for ultrasound integration was used to evaluate the combined ultrasound-CBCT system. Functionality included: connecting the probe to the system, loading calibration parameters, and allowing free-hand 3D ultrasound imaging. In Fig. 7 results for FRE and TRE (at the needle tip) are shown. The FRE (mean ± standard deviation) was 1.1 ± 0.5 mm for the vessel phantom, 1.3 ± 0.4 mm for the abdomen phantom, and (0.9 ± 0.3) mm for the lumbar phantom, consistent with the registration accuracy of the tracker. TRE at the needle tip was 2.3 ± 0.3 mm for the vessel phantom, 3.0 ± 0.4 mm for the abdomen phantom, and 2.1 ± 0.6 mm for the lumbar phantom.

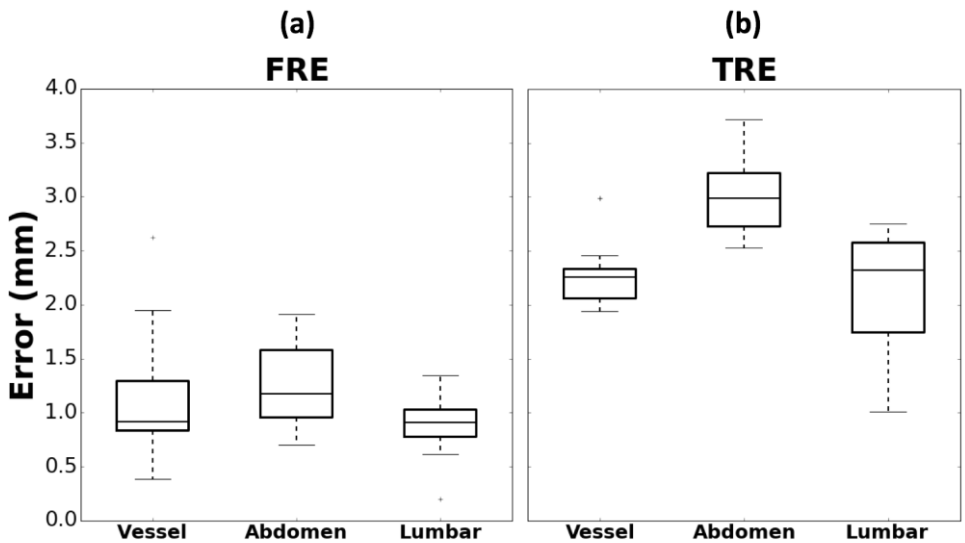

Fig. 7. Geometric accuracy of ultrasound-CBCT integration. (a) Fiducial Registration Error (FRE). (b) Target Registration Error (TRE), calculated at the needle tip for the vessel and abdomen phantoms and at the intersection of the needle with bone for the lumbar phantom.

Fig. 8 shows the ultrasound-CBCT registered images in the vicinity of the needle for the three cases evaluated: vessel, abdomen, and lumbar phantom. The registered images illustrate the utility of combined ultrasound and CBCT – the former providing real-time visualization, and the latter providing high-quality 3D imaging of soft-tissue and bone. In Fig. 8a,d,g a slice of the vessel phantom image is shown, where the needle is clearly visible within the simulated tissue, and the gradient CBCT image provides visualization of soft-tissue contrast corresponding to the inner part of the vessels. In Fig. 8b, the needle tip for the abdominal phantom case is conspicuous in the ultrasound plane (where the needle is seen to miss the simulated tumor). Finally, in Fig. 8c,f,i the ultrasound image shows the edge of the spine, while CBCT shows the complete bone structure and is exemplary of the potential benefit in combining both modalities – i.e., ultrasound performing real-time guidance and CBCT depicting the needle path inside the bone, where US contrast is limited by the technique.

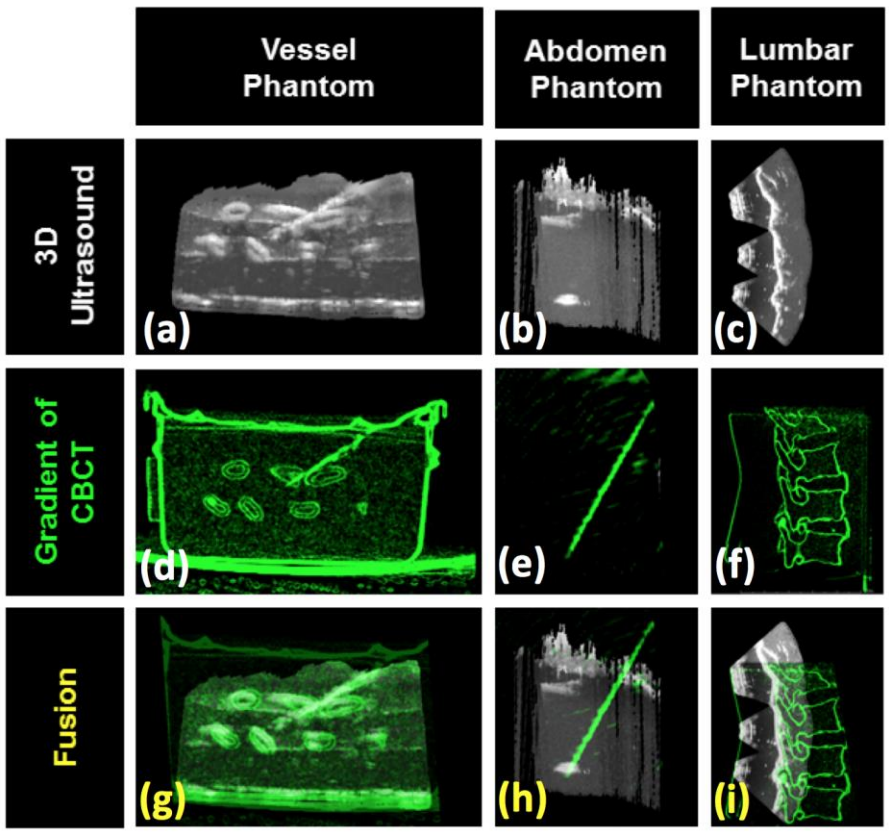

Fig. 8. Registration of free-hand 3D ultrasound with CBCT using fiducial-based registration. (a-c) Ultrasound image, (d-f) gradient of CBCT image, and (g-i) fusion of free-hand 3D ultrasound and CBCT gradient image for the Vessel, Abdomen, and Lumbar phantoms.

3.3. Image-based registration assessment

Results of the image-based registration are showed in Fig. 9, demonstrating that registration was feasible even with a low-cost ultrasound probe with limited image quality. Each of the similarity metrics maximizes at a solution that is within 1 mm and 1° of the tracker-based registration solution. Similarly, TRE is minimized at approximately the same solution. Errors in the localization of the needle tip during TRE estimation could cause the higher values of TRE in this example case (i.e., minimum TRE ~3.0-3.5 mm in Fig. 9 compared to ~2.0 - 3.0 mm in Fig. 7). Note that a perturbation factor of 0 also introduces random transformations. In cases studied, the NMI and MIND-Huber similarity metrics performed similar TRE minimum values, supporting their potential suitability for this multi-modality registration problem. The results are likely dependent on anatomical site and require validation in clinical image data, which is the subject of future work beyond this feasibility study.

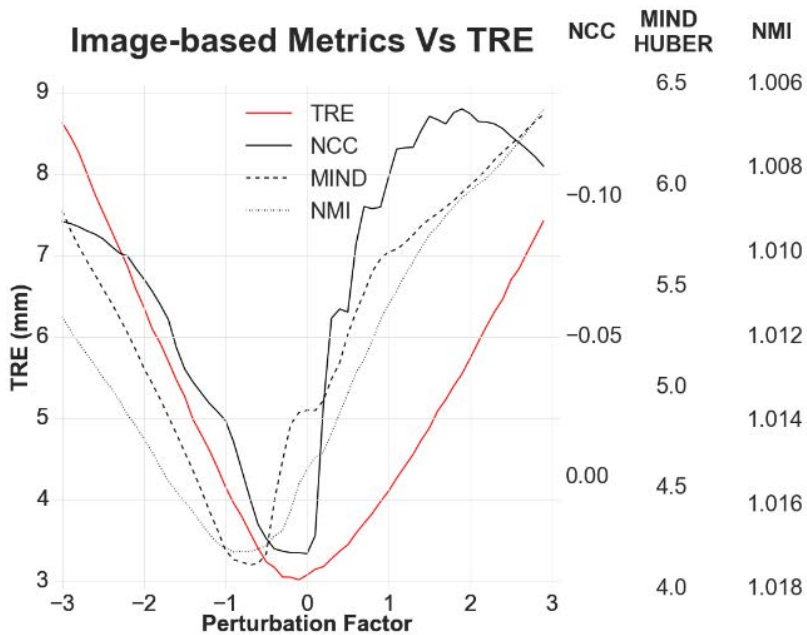

Fig. 9. Image-based registration of 3D ultrasound and CBCT. The TRE was measured as a function of Perturbation Factor, minimizing at the transformation taken as reference "truth." Three similarity metrics (NCC, NMI, and MIND-Huber) are each minimized within ~1 mm and ~1° of the reference.

4. Discussion and Conclusion

This paper presented the first image quality assessment for the Interson Vascular Access Probe VC 7.5 MHz and initial implementation of an integrated ultrasound-CBCT system for image-guided needle interventions. The low-cost ultrasound system showed modest image quality in terms of CNR and spatial resolution (PSF) and could be suitable for a variety of needle interventions within ~20–60 mm depth of the surface. Examples include superficial interventions such as arterial blood and thyroid biopsies, or obstetrics applications (Surbek et al., 2002) that could benefit from the competitive price and convenience of the system. Its small size, USB power supply, and low price could be suitable for environments with limited access to high-end imaging technology.

Development and feasibility of a free-hand 3D ultrasound imaging system registered with mobile C-arm CBCT was demonstrated. In the vessel phantom experiment, the system was able to track needle insertion in real-time due to ultrasound imaging that could be verified to hit the vessel target using CBCT. In the lumbar puncture experiment, the needle could be tracked to the surface of the spine using ultrasound, and the utility of the integrated system was evident in combination with CBCT capability to visualize the position of the needle in bone (Fig. 8i).The advantages of such US-CBCT integration is not limited to the potential clinical applications subject to the constraints of the US image quality characteristics of the Interson probe assessed in this study and could facilitate multi-modal image guidance capability to a wide variety of needle interventions with other suitable, higher-end US systems.

Needle-tip localization accuracy was ~2.1–3.0 mm (TRE) via the integrated ultrasound-CBCT system using fiducial-based registration. A limitation of this feasibility study is that we employed only two needles and only one insertion per phantom. However, we do not expect strong variability in TRE across the region of interest investigated in this work, given the fairly high number of registration fiducials (divots) surrounding the ROI (Fitzpatrick et al., 1998). This fairly high TRE was attributed primarily to the limited spatial resolution and CNR of the ultrasound probe that somewhat compromised the spatial calibration. The basic concept for ultrasound-CBCT system integration implemented here is compatible (without requiring additional development) with higher-end ultrasound systems with improved functionality and image quality, which would presumably enhance the ultrasound-to-tracker calibration and image-based registration.

Fiducials were placed surrounding the target on each case with different spatial distribution. Since the TRE depends in part on the distribution of fiducials around the target, the better the target is covered by fiducials the smaller the TRE is expected (Fitzpatrick et al., 1998). In the three studied cases, we found similar FRE values for each case (Fig. 7a). However, due in part to the differences in distribution of fiducials with respect to the target for each case (vessel, tumor and spine), the TRE was different among each phantom. Furthermore, the TRE also depends on the image quality – for the observer-based truth definition and directly for the registration-based approaches. The three phantoms presented distinct challenges with respect to both ultrasound and CBCT image quality, and the TRE was seen to vary accordingly. Finally, the acquisition of the 3D US image introduces some deformations on the phantom surface, presenting another potential source of variation in TRE.

Image-based registration results suggest that similarity metrics such as NCC or MIND-Huber are suitable objective functions for registration of these modalities. Image-based registration demonstrated estimated TRE < 4 mm for scenarios in which soft tissue was visible in both modalities and FOV was reasonably well covered by both modalities (i.e., ultrasound mosaicking holes were minimized). For the needle guidance task in these scenarios, initial work employed a rigid registration model; however, soft-tissue deformations due to the needle and/or ultrasound probe can be expected and warrants future investigation of nonrigid registration approaches – e.g., B-spline (Rueckert et al., 1999) or Demons (Nithiananthan et al., 2011; Vercauteren et al., 2009) transformations. On the other hand, surface-based registration schemes could also be employed in the US-CBCT registration context. Such strategies require a surface detection/segmentation processing (or surface markers). Alternatively, the surface markers could be visible directly in one modality (e.g., CBCT) and detected visually using a video camera mounted to / registered to the ultrasound probe. This amounts to a video-based analogue to the tracker-based approach demonstrated in this work. A good example is the Clear Guide system (Clear Guide Medical, Baltimore, MD, USA) for registration and fusion of ultrasound and CT/CBCT images. The results demonstrated above show the feasibility for ultrasound-CBCT image-based registration and motivate future work in which the tracker is used for construction of the free-hand 3D ultrasound volumes (and optionally for registration initialization), and accurate image-based registration is performed. Future research will include investigation of automatic image-based registration, including preclinical (cadaver or animal) studies to present more challenging imaging scenarios as well as realistic anatomical deformation patterns. The work reported above provides an important point of reference for future developments on automatic CT-to-ultrasound registration.

The TREK software architecture provided a flexible platform for development of modules for integrating the PLUS library with CBCT and surgical tracking. This work presented an integrated platform for needle guidance combining available open-source software tools and SDKs. Particular improvements to the PLUS toolkit were implemented regarding the ultrasound probe interface, including online tuning of acquisition

parameters during the procedure, thereby allowing more convenient tuning of image probe parameters that affect image quality.

The feasibility of integrated free-hand 3D ultrasound and mobile C-arm CBCT was demonstrated in phantom studies in scenarios emulating needle-based registration based on a low-cost ultrasound probe. The broad availability of low-cost ultrasound imaging systems with streamlined integration with fluoroscopy and CBCT could improve performance and safety in a variety of needle-based interventions.

Acknowledgements

This work was funded by NIH grant. R01-EB-017226, research partnership with Siemens XP (Erlangen, Germany), and grants TEC2013-48251-C2-1-R (Ministerio de Economía y Competitividad), DTS14/00192 (ISCIII), EU FP7 IRSES TAHITI (#269300), and FEDER funds.

Conflict of Interest: E. Marinetto declares that he has no conflict of interest. A. Uneri declares that he has no conflict of interest. T. de Silva declares that he has no conflict of interest. S. Reaungamornrat declares that he has no conflict of interest. W. Zbijewski declares that he has no conflict of interest. A. Sisniega declares that he has no conflict of interest. S. Vogt is an employee of Siemens Healthcare. G. Kleinszig is an employee Siemens Healthcare. J. Pascau declares that he has no conflict of interest. J. H. Siewerdsen has received research funding support from Siemens Healthcare.

References

Bachar, G., Siewerdsen, J.H., Daly, M.J., Jaffray, D.A., Irish, J.C., 2007. Image quality and localization accuracy in C-arm tomosynthesis-guided head and neck surgery. Med. Phys. 34, 4664–77.

Barker, E., Trimble, K., Chan, H., Ramsden, J., Nithiananthan, S., James, A., Bachar, G., Daly, M., Irish, J., Siewerdsen, J., 2009. Intraoperative use of cone-beam computed tomography in a cadaveric ossified cochlea model. Otolaryngol. Head. Neck Surg. 140, 697–702. doi:10.1016/j.otohns.2008.12.046

Boskovic, T., Stanic, J., Pena-Karan, S., Zarogoulidis, P., Drevelegas, K., Katsikogiannis, N., Machairiotis, N., Mpakas, A., Tsakiridis, K., Kesisis, G., Tsiouda, T., Kougioumtzi, I., Arikas, S., Zarogoulidis, K., 2014. Pneumothorax after transthoracic needle biopsy of lung lesions under CT guidance. J. Thorac. Dis. 6 Suppl 1, S99–S107. doi:10.3978/j.issn.2072-1439.2013.12.08

Brendel, B., Winter, S., Rick, a., Stockheim, M., Ermert, H., 2002. Registration of 3D CT and ultrasound datasets of the spine using bone structures. Comput. Aided Surg. 7, 146–155. doi:10.1002/igs.10038

Carbajal, G., Lasso, A., Gómez, A., Fichtinger, G., 2013. Improving N-wire phantom-based freehand ultrasound calibration. Int. J. Comput. Assist. Radiol. Surg. 8, 1063–72. doi:10.1007/s11548-013-0904-9

Chan, Y., Siewerdsen, J.H., Rafferty, M.A., Moseley, D.J., Jaffray, D.A., Irish, J.C., 2008. Cone-beam computed tomography on a mobile C-arm: novel intraoperative imaging technology for guidance of head and neck surgery. J. Otolaryngol. Head Neck Surg. 37, 81–90.

CHIN, K., PERLAS, A., CHAN, V., BRULL, R., 2008. Needle Visualization in Ultrasound-Guided Regional Anesthesia: Challenges and Solutions. Reg. Anesth. Pain Med. 33, 532–544. doi:10.1016/j.rapm.2008.06.002

Cleary, K., Peters, T.M., 2010. Image-guided interventions: technology review and clinical applications. Annu. Rev. Biomed. Eng. 12, 119–42. doi:10.1146/annurev-bioeng-070909-105249

Daly, M.J., Siewerdsen, J.H., Cho, Y.B., Jaffray, D.A., Irish, J.C., 2008. Geometric calibration of a mobile C-arm for intraoperative cone-beam CT. Med. Phys. 35, 2124–36.

Dang, H., Otake, Y., Schafer, S., Stayman, J.W., Kleinszig, G., Siewerdsen, J.H., 2012. Robust methods for automatic image-to-world

registration in cone-beam CT interventional guidance. Med. Phys. 39, 6484–98. doi:10.1118/1.4754589

Deguet, A., Kumar, R., Taylor, R., Kazanzides, P., 2008. The cisst libraries for computer assisted intervention systems. MIDAS J Syst Arch. Comput Assist Interv 1–8.

Fingerman, M., Benonis, J.G., Martin, G., 2009. A practical guide to commonly performed ultrasound-guided peripheral-nerve blocks. Curr. Opin. Anaesthesiol. 22, 600–607. doi:10.1097/ACO.0b013e32832f7643

Fitzpatrick, J.M., West, J.B., Maurer, C.R., 1998. Predicting error in rigid-body point-based registration. Med. Imaging, IEEE … 17, 694–702. doi:10.1109/42.736021

Hamming, N.M., Daly, M.J., Irish, J.C., Siewerdsen, J.H., 2009. Automatic image-to-world registration based on x-ray projections in cone-beam CT-guided interventions. Med. Phys. 36, 1800–12.

Heinrich, M.P., Jenkinson, M., Papiez, B.W., Brady, S.M., Schnabel, J.A., Papież, B.W., Brady, S.M., Schnabel, J.A., 2013. Towards Realtime Multimodal Fusion for Image-Guided Interventions Using Self-similarities. Lect. Notes Comput. Sci. (including Subser. Lect. Notes Artif. Intell. Lect. Notes Bioinformatics) 8149 LNCS, 187–194. doi:10.1007/978-3-642-40811-3_24

Huber, P.J., 1964. Robust Estimation of a Location Parameter. Ann. Math. Stat. 35, 73–101.

Khoury, A., Siewerdsen, J.H., Whyne, C.M., Daly, M.J., Kreder, H.J., Moseley, D.J., Jaffray, D.A., 2007. Intraoperative cone-beam CT for image-guided tibial plateau fracture reduction. Comput. Aided Surg. 12, 195–207. doi:10.3109/10929080701526872

Kitware Inc., n.d. IntersonSDKCxx [WWW Document]. IntersonSDKCxx. URL https://github.com/KitwareMedical/IntersonSDKCxx

Koukourakis, G., Kelekis, N., Armonis, V., Kouloulias, V., 2009. Brachytherapy for prostate cancer: a systematic review. Adv. Urol. 327945. doi:10.1155/2009/327945

Lamperti, M., Bodenham, A.R., Pittiruti, M., Blaivas, M., Augoustides, J.G., Elbarbary, M., Pirotte, T., Karakitsos, D., LeDonne, J., Doniger, S., Scoppettuolo, G., Feller-Kopman, D., Schummer, W., Biffi, R., Desruennes, E., Melniker, L.A., Verghese, S.T., 2012. International evidence-based recommendations on ultrasound-guided vascular access. Intensive Care Med. 38, 1105–1117. doi:10.1007/s00134-012-2597-x

Lasso, A., Heffter, T., Rankin, A., Pinter, C., Ungi, T., Fichtinger, G., 2014. PLUS: open-source toolkit for ultrasound-guided intervention systems. IEEE Trans. Biomed. Eng. 1–11. doi:10.1109/TBME.2014.2322864

Lee, S., Gallia, G.L., Reh, D.D., Schafer, S., Uneri, A., Mirota, D.J., Nithiananthan, S., Otake, Y., Stayman, J.W., Zbijewski, W., Siewerdsen, J.H., 2012. Intraoperative C-arm cone-beam computed tomography: quantitative analysis of surgical performance in skull base surgery. Laryngoscope 122, 1925–32. doi:10.1002/lary.23374

Maier-Hein, L., Tekbas, A., Seitel, A., Pianka, F., Müller, S.A., Satzl, S., Schawo, S., Radeleff, B., Tetzlaff, R., Franz, A.M., Müller-Stich, B.P., Wolf, I., Kauczor, H.-U., Schmied, B.M., Meinzer, H.-P., 2008. In vivo accuracy assessment of a needle-based navigation system for CT-guided radiofrequency ablation of the liver. Med. Phys. 35, 5385–96. doi:10.1118/1.3002315

MD, S.F.C., MD, L.C.C., MBA, U.M.H.M.D., 2014. The Role of Sonography in Thyroid Cancer. Radiol. Clin. NA 52, 1283–1294. doi:10.1016/j.rcl.2014.07.007

Muratore, D.M., Russ, J.H., Dawant, B.M., Galloway, R.L., 2002. Three-dimensional image registration of phantom vertebrae for image-guided surgery: a preliminary study. Comput. Aided Surg. 7, 342–52. doi:10.1002/igs.10055

Neshat, H., Cool, D.W., Barker, K., Gardi, L., Kakani, N., Fenster, A., 2013. A 3D ultrasound scanning system for image guided liver interventions. Med. Phys. 40, 112903. doi:10.1118/1.4824326

Nithiananthan, S., Schafer, S., Mirota, D.J., Stayman, J.W., Zbijewski, W., Reh, D.D., Gallia, G.L., Siewerdsen, J.H., 2012. Extra-dimensional Demons: a method for incorporating missing tissue in deformable image registration. Med. Phys. 39, 5718–31. doi:10.1118/1.4747270

Nithiananthan, S., Schafer, S., Uneri, A., Mirota, D.J., Stayman, J.W., Zbijewski, W., Brock, K.K., Daly, M.J., Chan, H., Irish, J.C., Siewerdsen, J.H., 2011. Demons deformable registration of CT and cone-beam CT using an iterative intensity matching approach. Med. Phys. 38, 1785. doi:10.1118/1.3555037

Nolsøe, C., Nielsen, L., Torp-Pedersen, S., Holm, H.H., 1990. Major complications and deaths due to interventional ultrasonography: a review of 8000 cases. J. Clin. Ultrasound 18, 179–84.

Pieper, S., Halle, M., Kikinis, R., 2004. 3D Slicer. 2004 2nd IEEE Int. Symp. Biomed. Imaging Nano to Macro (IEEE Cat No. 04EX821) 2, 632–635. doi:10.1109/ISBI.2004.1398617

Reaungamornrat, S., Liu, W.P., Wang, A.S., Otake, Y., Nithiananthan, S., Uneri, A., Schafer, S., Tryggestad, E., Richmon, J., Sorger, J.M., Siewerdsen, J.H., Taylor, R.H., 2013. Deformable image registration for cone-beam CT guided transoral robotic base-of-tongue surgery. Phys. Med. Biol. 58, 4951–79. doi:10.1088/0031-9155/58/14/4951

Roeder, F., Schramm, O., Timke, C., Habl, G., Tanner, M.C., Huber, P.E., 2010. Postplanning of a three-dimensional dose distribution for intraoperative electron radiation therapy (IOERT) using intraoperative C-arm based 3D-imaging – a phantom study, in: Int J CARS, 5 (Suppl. 1. pp. S71–S72.

Rudzinski, J.K., Kawakami, J., 2014. Incidence of infectious complications following transrectal ultrasound-guided prostate biopsy in Calgary, Alberta, Canada: A retrospective population-based analysis. Can. Urol. Assoc. J. 8, E301-5. doi:10.5489/cuaj.1751

Rueckert, D., Sonoda, L.I., Hayes, C., Hill, D.L.G., Leach, M.O., Hawkes, D.J., 1999. Nonrigid registration using free-form deformations: application to breast MR images. IEEE Trans. Med. Imaging 18, 712–721. doi:10.1109/42.796284

Schafer, S., Nithiananthan, S., Mirota, D.J., Uneri, A., Stayman, J.W., Zbijewski, W., Schmidgunst, C., Kleinszig, G., Khanna, A.J., Siewerdsena, J.H., 2011. Mobile C-arm cone-beam CT for guidance of spine surgery: image quality, radiation dose, and integration with interventional guidance. Med. Phys. 38, 4563–74.

Schafer, S., W. Stayman, J., Zbijewski, W., Schmidgunst, C., Kleinszig, G., H. Siewerdsen, J., Stayman, J.W., Zbijewski, W., Schmidgunst, C., Kleinszig, G., Siewerdsen, J.H., 2012. Antiscatter grids in mobile C-arm cone-beam CT: effect on image quality and dose. Med. Phys. 39, 153–9. doi:10.1118/1.3666947

Showalter, S.L., Petroni, G., Trifiletti, D.M., Libby, B., Schroen, A.T., Brenin, D.R., Dalal, P., Smolkin, M., Reardon, K.A., Showalter, T.N., 2016. A Novel Form of Breast Intraoperative Radiation Therapy With CT-Guided High-Dose-Rate Brachytherapy: Results of a Prospective Phase 1 Clinical Trial. Int. J. Radiat. Oncol. Biol. Phys. 96, 46–54. doi:10.1016/j.ijrobp.2016.04.035

Siewerdsen, J.H., Moseley, D.J., Burch, S., Bisland, S.K., Bogaards, A., Wilson, B.C., Jaffray, D.A., 2005. Volume CT with a flat-panel detector on a mobile, isocentric C-arm: pre-clinical investigation in guidance of minimally invasive surgery. Med. Phys. 32, 241–54.

Surbek, D. V., Young, A., Danzer, E., Schoeberlein, A., Dudler, L., Holzgreve, W., 2002. Ultrasound-guided stem cell sampling from the early ovine fetus for prenatal ex vivo gene therapy. Am. J. Obstet. Gynecol. 187, 960–963. doi:10.1067/mob.2002.126982

Tiong, L., Maddern, G.J., 2011. Systematic review and meta-analysis of survival and disease recurrence after radiofrequency ablation for hepatocellular carcinoma. Br. J. Surg. 98, 1210–24. doi:10.1002/bjs.7669

Uneri, A., Nithiananthan, S., Schafer, S., Otake, Y., Stayman, J.W., Kleinszig, G., Sussman, M.S., Prince, J.L., Siewerdsen, J.H., 2013. Deformable registration of the inflated and deflated lung in cone-beam CT-guided thoracic surgery: initial investigation of a combined model- and image-driven approach. Med. Phys. 40, 17501. doi:10.1118/1.4767757

Uneri, A., Schafer, S., Mirota, D.J., Nithiananthan, S., Otake, Y., Taylor, R.H., Gallia, G.L., Khanna, A.J., Lee, S., Reh, D.D., Siewerdsen, J.H., 2012. TREK: an integrated system architecture for intraoperative cone-beam CT-guided surgery. Int. J. Comput. Assist. Radiol. Surg. 7, 159–73. doi:10.1007/s11548-011-0636-7

Vercauteren, T., Pennec, X., Perchant, A., Ayache, N., 2009. Diffeomorphic demons: Efficient non-parametric image registration. Neuroimage 45, S61–S72. doi:10.1016/j.neuroimage.2008.10.040

Wang, A.S., Stayman, J.W., Otake, Y., Kleinszig, G., Vogt, S., Gallia, G.L., Khanna, A.J., Siewerdsen, J.H., 2014. Soft-tissue imaging with C-arm cone-beam CT using statistical reconstruction. Phys. Med. Biol. 59, 1005–26. doi:10.1088/0031-9155/59/4/1005

Wein, W., Brunke, S., Khamene, A., Callstrom, M.R., Navab, N., 2008. Automatic CT-ultrasound registration for diagnostic imaging and image-guided intervention. Med. Image Anal. 12, 577–585. doi:10.1016/j.media.2008.06.006

Wermker, K., Kleinheinz, J., Jung, S., Dirksen, D., 2014. Soft tissue response and facial symmetry after orthognathic surgery. J. Craniomaxillofac. Surg. doi:10.1016/j.jcms.2014.01.032

Yan, C.X.B., Goulet, B., Tampieri, D., Collins, D.L., 2012. Ultrasound-CT registration of vertebrae without reconstruction. Int. J. Comput. Assist. Radiol. Surg. 7, 901–909. doi:10.1007/s11548-012-0771-9

Yaniv, Z., Cheng, P., Wilson, E., Popa, T., Lindisch, D., Campos-Nanez, E., Abeledo, H., Watson, V., Cleary, K., Banovac, F., 2010. Needle-based interventions with the image-guided surgery toolkit (IGSTK): from phantoms to clinical trials. IEEE Trans. Biomed. Eng. 57, 922–33. doi:10.1109/TBME.2009.2035688

Zhu, Y., Magee, D., Ratnalingam, R., Kessel, D., 2007. A training system for ultrasound-guided needle insertion procedures. Med. Image

Comput. Comput. Assist. Interv. 10, 566–74.